INVITED PAPER

Hybrid 3-D-Printing Technology for Tunable THz Applications

In this paper, a hybrid manufacturing approach is presented that combines metallized passive components produced through the polymer-jetting process with active semiconductor devices. The potential for producing low-cost THz communication systems using this methodology is demonstrated with the successful development of a THz I-Q vector modulator.

By William J. Otter *Member, IEEE*, and Stepan Lucyszyn *Fellow, IEEE*

ABSTRACT | In recent years, additive manufacturing has experienced rapid growth, due to its inherent capabilities for creating arbitrary 3-D structures, accessibility, and associated low manufacturing costs. This paper first reviews the state of the art in 3-D printing for terahertz (THz) applications and identifies the critical features required for such applications. The future potential for this technology is demonstrated experimentally with the first 3-D-printed, optically controlled THz IQ vector modulator. Here, miniature high-resistivity silicon implants are integrated into metal-pipe rectangular waveguides. The 3-D-printed split-block assembly also houses two packaged infrared laser diodes and a heat sink. The measured performance of a proof-of-principle 4-quaternary amplitude modulation (4-QAM) vector modulator that operates up to 500 GHz is reported. This new hybrid 3-D printing THz technology, which combines semiconductor devices with potentially low-cost, high-performance passive guided-wave structures represents a paradigm shift and may prove to be an ideal solution for implementing affordable transceivers in future ubiquitous THz applications.

KEYWORDS | Additive manufacturing; fused deposition modeling (FDM); metal-pipe rectangular waveguide (MPRWG); optoelectronics; Polyjet; quaternary amplitude modulation (QAM); silicon; selective laser melting (SLM); selective laser sintering (SLS); stereolithographic apparatus (SLA); terahertz (THz); 3-D printing; vector modulator

I. INTRODUCTION

The conventional terahertz (THz) frequency range, from 100 GHz to 10 THz, is rapidly being developed for commercial exploitation [1]. Historically, the THz spectrum is also known as the submillimeter-wave band [by the radio frequency (RF) community] and far-infrared (by the optics community). Until relatively recently, the THz spectrum has been mainly used by the scientific community for radio astronomy [2], [3]. This application has been the key driver for THz optics, antennas, detectors, and associated guided-wave interconnects, while a THz gap has developed in associated source generators [4] and modulators. Closing this gap has been an active area of THz research in recent years, with significant advances being made in performance (e.g., >1 W, achieved with quantum cascade lasers [5] and higher power multipliers [6]). However, little has been demonstrated in the area of low-cost tunable front-end control components for ubiquitous THz applications.

Today, with the potential for real commercial exploitation, the THz spectrum is opening up to new applications; including nondestructive testing, security, and communications. For example, with nondestructive testing, the THz frequency range has been used for inspecting artwork [7],

Manuscript received July 27, 2016; revised September 30, 2016; accepted November 7, 2016. Date of publication December 23, 2016; date of current version March 20, 2017.This work was supported by the U.K. Engineering and Physical Sciences Research Council, under Grant EP/M001121/1 "TERACELL."
The authors are with the Centre for THz Science and Engineering and also the Optical and Semiconductor Devices Group, Department of Electrical and Electronic Engineering, Imperial College London, London SW7 2AZ, U.K.
(e-mail: w.otter@imperial.ac.uk; s.lucyszyn@imperial.ac.uk).

Digital Object Identifier: 10.1109/JPROC.2016.2629958

the coating thickness of pharmaceutical tablets [8], and paint thickness within the automotive industry [9]. In security, below *ca*. 600 GHz, it is possible to detect and in some cases identify concealed weapons [10] and illegal contraband [11] hidden underneath clothing. As lower frequency bands have become ever more crowded, communications systems are moving up in frequency, providing the opportunity for terabit-per-second links [12].

For all these applications, guided-wave structures are required, for either implementing a specific function (e.g., resonating, phase shifting, power coupling, etc.) or as an associated interconnect. Common technologies used at microwave frequencies include microstrip, stripline, and coaxial cable. However, the inherent high attenuation (due to excess current densities associated with the small cross-sectional areas of the signal line) and high manufacturing costs limit their use at THz frequencies. Alternatively, optical fibers and quasi-optical technologies do not lend themselves to compact integrated solutions at THz frequencies. The metal-pipe rectangular waveguide (MPRWG) offers both relatively low attenuation and compatibility with modular integrated solutions at THz frequencies [13–15]. For example, at 600 GHz, a high-quality microstrip transmission line may be expected to have a dissipative attenuation of ~1 dB/mm, while an MPRWG would be at least an order of magnitude lower. For this reason, there now exist IEEE standards for MPRWGs and their flanges for frequencies up to 5 THz [16]–[18].

Traditionally, THz MPRWGs have been machined in one of four ways: 1) drawing (reshaping) a metal pipe across a rectangular die; 2) computer numerically controlled (CNC) milling of a split-block die; 3) electronic discharge machining (spark erosion); and 4) electroforming a mandrel, which is subsequently selectively etched away. In addition to machining, other technologies also exist; these include the bulk micromachining of silicon [19] and surface micromachining in SU8, with additional assembly/packaging [20],[21].

II. REVIEW OF 3-D PRINTING FOR THZ APPLICATIONS

A. Generic 3-D Printing Technologies

Commercial manufacturing technologies for MPRWGs impose limits on design complexity and result in high unit cost components. Over the past two decades, 3-D printing (or additive layer manufacturing) technology has seen a dramatic improvement in resolution, while associated costs have also reduced. Moreover, in recent years, high-performance 3-D-printed RF components and MPRWG have been demonstrated [22]–[24]. These advances have shown the disruptive nature of 3-D printing, for the following five key reasons.

1) Complexity: Structures can be realized monolithically in ways not possible with traditional manufacturing techniques. This is especially important for part dimensions at the lower bound of CNC capabilities, where assembly tolerances start to dominate the total error in dimensions. Moreover, highly complex structures can be realized in a single print operation.
2) Weight: Components are lightweight with polymer-based building materials, e.g., a 3-D-printed MPRWG operating at X-band (8–12 GHz) can be a third of the weight of its commercially available machined counterpart [22], although this weight advantage may not be significant at terahertz frequencies.
3) Speed: A highly complex 3-D-printed component can be realized within hours.
4) Cost: Three-dimensional printing can be ultralow cost for small production runs, making it ideal for prototyping.
5) Accessibility: A general 3-D printer can be used for many diverse applications (i.e., not just for making THz components) and so they will, in time, become ubiquitous.

There are four generic classes of 3-D printing technologies: 1) fused deposition modeling (FDM); 2) stereolithographic apparatus (SLA); 3) polymer-jetting (Polyjet); and 4) selective laser sintering/melting (SLS/SLM). These different manufacturing processes have distinct properties that make them useful for different components, but also limit the MPRWG frequency of operation. For THz MPRWGs, the minimum printable feature size and relative surface roughness are critical parameters for achieving single-mode operation and high performance, respectively.

In this section, based on the different generic 3-D printing technologies, a review of exemplars for THz applications will be given.

B. Fused Deposition Modeling (FDM)

FDM printing selectively deposits an extruded thermoplastic, representing a relatively inexpensive process and an ideal entry-level technology. However, FDM provides the lowest spatial resolution 3-D printing method, with build layer heights from 50 to 500 μm; resolution is limited (typically to 100 μm) by nozzle size [22]. Moreover, with common materials, it is a relatively slow printing process when compared with other 3-D printing methods such as Polyjet. Furthermore, material shrinkage must be taken into account. Because of limitations in spatial resolution, at present, there are few FDM examples of THz components that can be reported. One exception was recently reported by Busch *et al.* at the Universität Marburg (Marburg, Germany) [25]. They studied the absorption coefficient and refractive index properties of seven thermoplastics: acrylonitrile butadiene styrene (ABS), polylactic acid (PLA), nylon, Bendlay, high-density polyethylene (HDPE), polypropylene (PP), and polystyrene. As seen in Fig. 1(a), HDPE and PP have the lowest losses. Unfortunately, neither one is suitable for FDM printing, as both are very soft and their temperature coefficient of expansion is high. However, the relatively low loss properties of polystyrene were used to demonstrate collimating lenses, having focal lengths of 55 and 90 mm, between 205 and 527 GHz, as shown in Fig. 1(b).

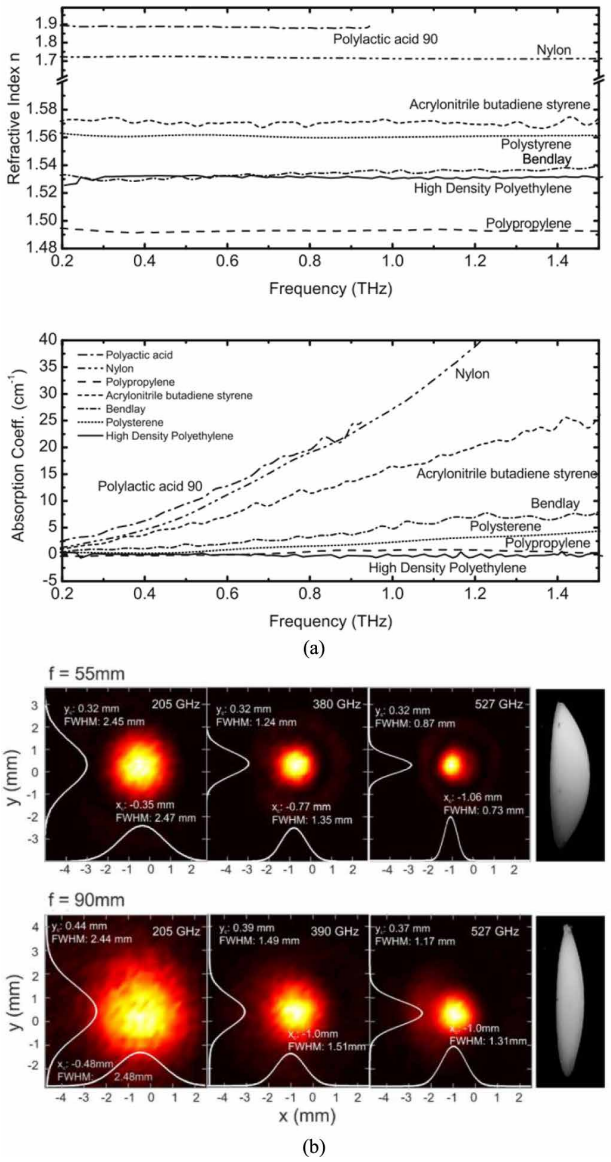

Fig. 1. ***FDM-printed THz technologies: (a) material properties; and (b) measured spot sizes for two collimating polystyrene lenses [25]. Springer, reprinted with permission.***

In addition, holographic lenses have been demonstrated for imaging at 0.3 THz [26].

A woodpile electromagnetic bandgap structure was demonstrated by Lee *et al.* at Queen Mary, University of London (London, U.K.). This ceramic paste extrusion process is used to form the woodpile that is then heated for debinding and sintering. The measured results show a bandgap of 90–105 GHz [27].

C. Stereolithographic Apparatus (SLA)

SLA printers use an ultraviolet (UV) curable resin that is exposed with a specific pattern for each print layer, defined either by a laser beam above or a projector below the build plane. This process can achieve much greater resolution, when compared to FDM, as SLA is limited by the small spot size of the laser or spatial resolution of the projector. It is expected that with future development, micrometer-level accuracy can be achieved that is commensurate with micromachining and microelectromechanical system (MEMS) technologies [28].

At the lower end of the THz spectrum, an MPRWG was demonstrated by Timbie *et al.* at the University of Wisconsin (Madison, WI, USA), with a 0.3-dB insertion loss at W-band [29]. Furthermore, a split-block MPRWG has been developed by Imperial College London (London, U.K.), seen in Fig. 2(a) [22]. A worst case return loss of ~21 dB and a dissipative attenuation of 11 dB/m at 110 GHz was measured at the U.K. National Physical Laboratory (NPL). This performance is comparable to a copper machined MPRWG having a worst case return loss of ~36 dB and a dissipative attenuation of 10 dB/m at 110 GHz, seen in Fig. 2(b) and (c), respectively. The same technology was then used to demonstrate a sixth-order Chebyshev inductive iris bandpass filter, shown in Fig. 2(d), having a center frequency f_o = 107.2 GHz and 3-dB bandwidth Δf = 6.8 GHz seen in Fig. 2(e). Here, a center-frequency insertion loss of only $-20\log_{10}|S_{21}(f_o)|$ = 0.95 dB was measured at NPL, demonstrating an associated unloaded quality factor of 152.

The private company SWISSto12, a spin-off of the Swiss Federal Institute of Technology Lausanne (EPFL, Lausanne, Switzerland), 3-D-printed metal coated plastic (MCP) waveguides and diagonal pyramidal horn antennas [30]–[32]. Examples include WR-3.4 band (220–330 GHz) MPRWGs and associated pyramidal horn antenna, shown in Fig. 3; the former exhibits a minimum dissipative attenuation of 12 dB/m at *ca.* 280 GHz. These waveguides are first printed with a 25-μm layer height and then mechanically and chemically finished, before being electroless plated with copper and flash coated in gold. In addition, WR-5.1 band (140–220 GHz) straight and S-bend MPRWG sections are being marketed by SWISSto12 for use in applications such as on-wafer probing.

D. Polymer Jetting

Polyjet printing provides state-of-the-art resolution in the 3-D printing of plastics. It involves the jetting of photopolymers from multiple nozzles to form each layer of the print. The photopolymer is immediately UV cured by the print head.

THz applications of this technology were demonstrated at the University of Arizona (Tucson, AZ, USA) by Wu *et al.* [33], [34]. They initially developed a hollow electromagnetic bandgap waveguide formed from a triangular lattice of cylindrical air holes within a 3-D-printed lattice structure. A waveguide defect was added by removal of plastic from the inner core, as seen in Fig. 4(a). At 105 GHz, a dissipative attenuation of 30 dB/m was measured [33]. Using the same technology, a 146-GHz horn antenna was demonstrated [34]. The antenna has a measured 10 half-power beamwidth and first sidelobe suppression of 20 dB at 146 GHz. More recently, in

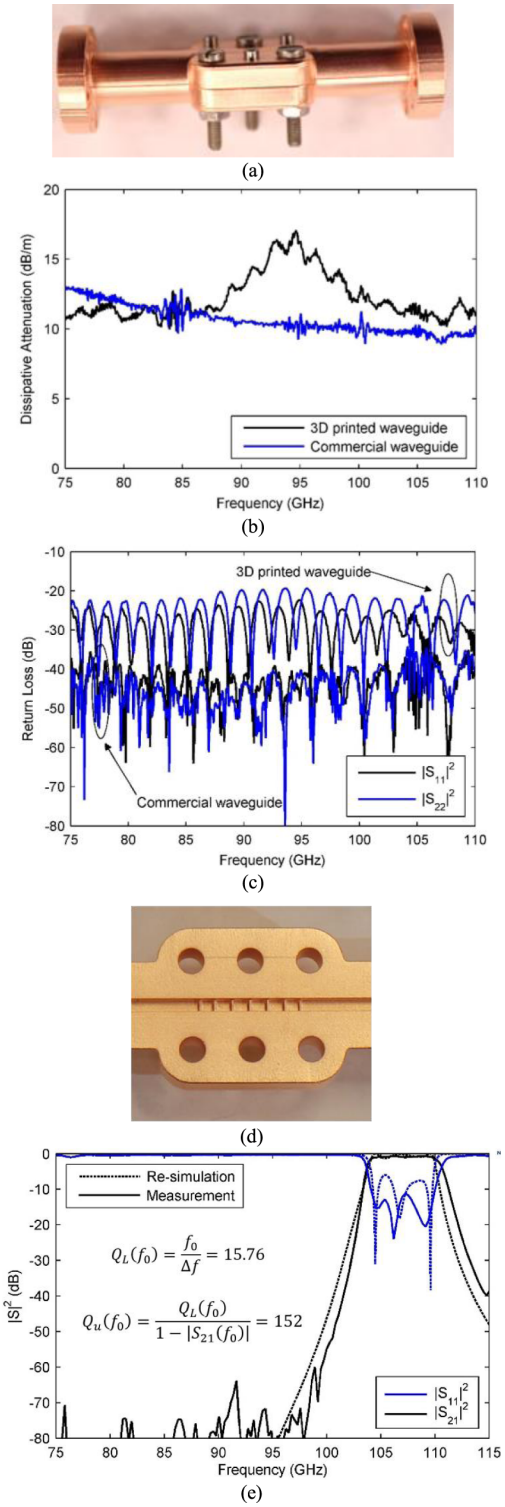

Fig. 2. *SLA-printed THz MPRWG [22]: (a) assembled split-block thu line; (b) measured thu-line dissipative attenuation comparison with conventional machined waveguide; (c) measured thu-line return loss comparison with conventional machined waveguide; (d) one half of a split-block sixth-order Chebyshev inductive iris bandpass filter; and (e) measured and resimulated responses of the filter in (d). The loaded and unloaded quality factors $Q_L(f_o)$ and $Q_u(f_o)$, respectively, of the filter are indicated. IEEE, reprinted with permission.*

Fig. 3. *SLA-printed SWISSto12 WR-3.4 band MCP waveguide technology [32]: thru line (left), pyramidal horn antenna (center) and 90 bend (right). SWISSto12, reprinted with permission.*

2014, the same team demonstrated high gain dielectric reflect arrays at 100 GHz [35]. Qu *et al.* at the University of Electronic Science and Technology of China (UESTC, Chengdu, China), using the same technology, has demonstrated a high gain lens antenna operating at 275 GHz [36].

E. Selective Laser Sintering/Melting

The previous technologies generally print polymer materials, which may then require subsequent metallization. Different approaches for plating include: 1) evaporation deposition; 2) sputter coating; 3) electroless plating; or 4) silver dip coating. In contrast, with SLS/SLM, components are printed directly in metal (e.g., copper). Similarly to SLA printing, the part is defined by a laser pattern of light that either sinters or melts metal particles together. The component is built up on a platform that lowers; after each layer is built, a new layer of metal powder is rolled over the surface and the process is repeated. The resolution of these prints is ultimately defined by the metal particle size.

The Catholic University of Leuven (Leuven, Belgium), Caekenberghe *et al.* demonstrated a W-band 50-mm-long SLM MPRWG made from a Ti-6Al-4V alloy. Measured results demonstrate a loss of 29 dB/m at 110 GHz [37].

At Chalmers University (Chalmers, Sweden), Zhang *et al.* [38] demonstrated D-band (110–170 GHz) and H-band (220–325 GHz) MPRWGs, made from a $CuSn_{15}$ powder having a particle size of <20 μm. The waveguides are printed in a single piece (i.e., not as a split block, normally associated with polymer-based 3-D printing of THz MPRWGs, as additional metal

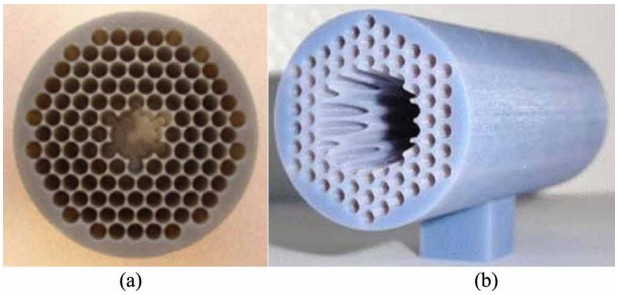

Fig. 4. *Polyjet-printed electromagnetic crystal (EMXT) components: (a) 105-GHz waveguide [33]; and (b) 146-GHz horn antenna [34]. IEEE, reprinted with permission.*

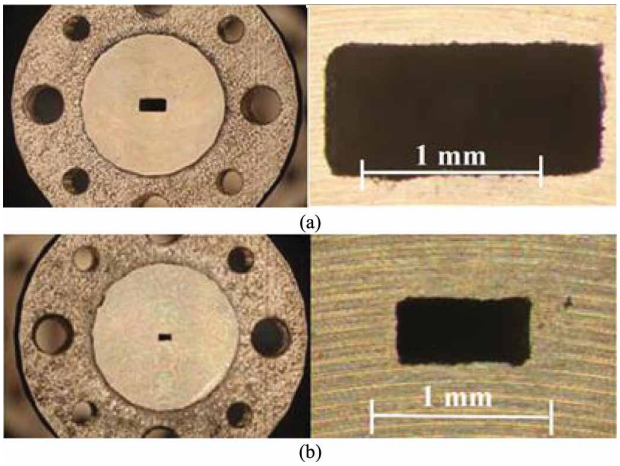

Fig. 5. ***SLM-printed THz MPRWGs after postprocessing, with views of the flange (left) and close-up views of the rectangular waveguides aperture (right) [38]: (a) D-band; and (b) H-band. IEEE, reprinted with permission.***

plating was not needed). However, significant postprocessing of the components was still required; alignment holes and screw threads were drilled in and the flanges were made smooth by milling, not required with the previous polymer-based 3-D printing exemplars. Here, milling of the flange was required due to the print finish having a significant surface roughness of ~6 μm. Within the waveguide, the components are cleaned to ensure there is no powder remaining, but no internal polishing is undertaken. Images of the final flanges, with close-up views of the rectangular waveguides aperture, for the D-band and H-band MPRWGs can be seen in Fig. 5(a) and (b), respectively. A dissipative attenuation of 19 and 94 dB/m is reported for the D-band and H-band MPRWGs, respectively.

Using the same technology, conical horn antennas were demonstrated, operating in the D-band and H-band, with gains of 22.0 and 21.5 dBi, respectively, having a return loss of more than 20 dB across the bands [39]. An additional step of postprocessing was used on the horns to polish the internal surfaces. The micromachined process (MMP) uses abrasive particles contained within a high-pressure fluid to reduce the internal surface roughness of the print, from 6 down to 0.25 μm. This brings a significant performance gain for SLM-printed THz components, but increases the manufacture time and doubles the cost of manufacture.

Fig. 6. ***SLM-printed THz conical horn antennas with MPRWG flanges after postprocessing: D-band (top) and H-band (bottom) [39]. IEEE, reprinted with permission.***

F. Surface Roughness Limitations for THz Applications

Tischer [40], [41] and Huang *et al.* [42] demonstrated through measurements and simulations, respectively, how surface properties adversely affect performance at THz frequencies. Surface roughness will increase insertion loss significantly, due to the increase in the effective surface resistance of the internal waveguide walls. High grade commercial coin silver waveguides exhibit a 5%–15% increase in attenuation, when compared to theoretical values of coined silver for a perfectly smooth waveguide up to 200 GHz. Moreover, it has been shown experimentally that an internal surface roughness of 1 μm can increase the surface resistance by up to 30%, when compared to a highly polished waveguide. In addition, the presence of surface roughness increases the waveguide's cutoff frequency.

Examples of surface roughness for the three polymer-based 3-D printing technologies are shown in Fig. 7. Scalloping in the direction of build can be clearly seen with the FDM sample in Fig. 7(a). This gives a peak surface roughness of $\pm$13 μm in the direction of build [22], limiting this technology to microwave frequencies when creating MPRWG-based structures. The SLA sample in Fig. 7(b) has a peak surface roughness of $\pm$3 μm, making it suitable for applications up to the lower THz range [22]. However, it should be noted, by observing the added white demarcation line (between the internal sidewall and base of the waveguide), that there are significant deviations from a straight sidewall, potentially reducing the maximum frequency of operation. A Polyjet sample is shown in Fig.7(c). It can be seen that there is less deviation from the ideal straight sidewall and a significantly smoother surface finish.

The sample in Fig. 7(c) represents the first reported 3-D-printed THz MPRWG to cover the WR-2.2 band (325–500 GHz). Preliminary measurements for this nonoptimized Polyjet exemplar give an average insertion loss of 11 dB for a 25-mm thru line. This high insertion loss is due to the significant surface roughness. While excessive, the poor insertion loss performance is not inherent to Polyjet printing; next-generation printers and their associated materials will result in much lower levels of surface roughness, which will dramatically improve component performance and push up the THz frequency of operation.

Finally, SLS/SLM printing suffers from more significant surface roughness. This is seen in Fig. 7(d) and (f), where nylon, alumide, and polyamide prints are shown, respectively. Surface roughness is apparent, with measured particulate sizes of ~30 μm with both alumide and polyamide, making them unsuitable for THz applications. Zhang *et al.* have demonstrated that with suitable polishing (mechanically and/or chemically) a surface roughness of 0.25 μm can be achieved [39]. A comparison of dissipative attenuation for THz MPRWGs, manufactured using (micro)machining and 3-D printing technologies is shown in Table 1.

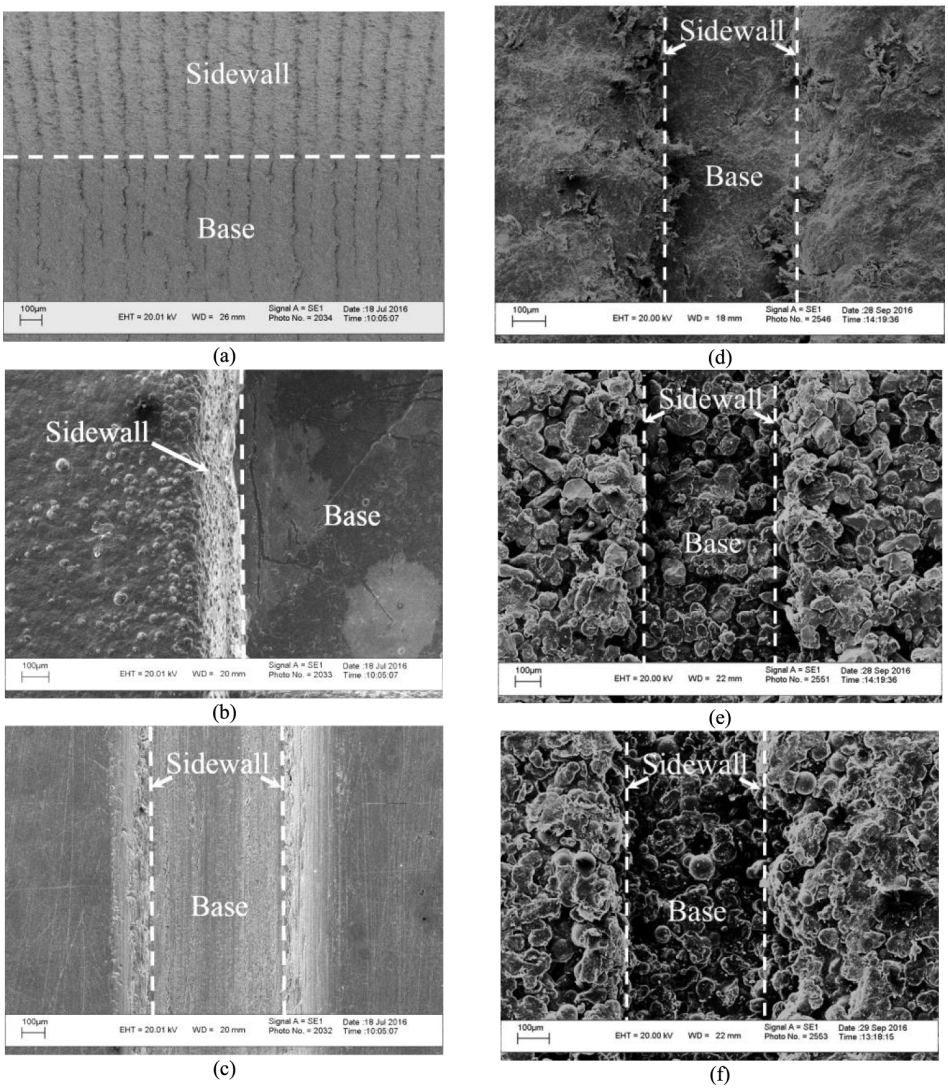

Fig. 7. ***Scanning electron micrographs for polymer-based 3-D-printed MPRWGs: (a) FDM X-band (8–12 GHz); (b) SLA W-band (75–110 GHz); (c) Polyjet WR-2.2 (325–500 GHz); (d) SLS nylon WR-2.2; (e) SLS Alumide WR 2-2; and (f) SLS polyamide WR-2.2. These images show the internal waveguide walls; the dashed white demarcation lines are added to indicate the corner between the sidewall and base of the rectangular waveguides.***

III. TUNABLE THZ COMPONENTS

Tunable front-end components are critical for optimized systems level performance. Of fundamental importance are: 1) amplitude control, via a variable attenuator; 2) phase control, via a phase shifter; and 3) combined amplitude-phase control, via a vector modulator. These components find applications in high-performance communications, radar, and measurement systems; for example, in the beam forming networks of phased-array antennas, power amplifier linearizers or at-carrier frequency modulators. However, implementing variable attenuators, phase shifters, and vector modulators becomes more technologically challenging and expensive as frequency increases. Indeed, there are few examples of ultrabroadband solutions that operate at THz frequencies.

At the lower end of the THz band, Imperial College London demonstrated an optically controlled photonic crystal variable attenuator [47]. By controlling the photogeneration of electron–hole pairs, within high-resistivity silicon (HRS), the authors demonstrated a dynamic range >45 dB over the 92–102-GHz bandwidth. At 110 GHz, McPherson *et al.* [48] demonstrated an electronically tunable monolithic microwave integrated circuit (MMIC) in-phase/quadrature-phase (IQ) vector modulator, demonstrating 64-quaternary amplitude modulation (64-QAM) digital modulation directly at the carrier frequency, intended for implementing miniature software-controlled transmitters. Recently, a 275-GHz MMIC phase shifter was reported by Quan *et al.* [49], demonstrating a

Table 1 Comparison of Published THz MPRWG Measured Attenuation Performances

Waveguide Band	Frequency (GHz)	Manufacturing Technology	Split Block	Waveguide Filler	Attenuation dB/m	Attenuation dB/λ_g	Ref
WR-10	100	Bulk micromachined	Yes	Air	-	0.05	[39]
WR-10	105	Surface micromachined	No	Polyimide	8,660	44	[40, 41]
WR-10	75-110	CNC machined	Yes	Air	4	-	[42]
WR-10	75-110	Surface micromachined	Yes	Air	-	0.5	[20]
WR-10	110	Machined	No	Air	10	0.032	-
WR-10	110	3D printed (SLA)	Yes	Air	11	0.036	[22]
WR-06	110-170	3D printed (SLM)	No	Air	18.96	-	[34]
WR-06	110-170	Commercial	No	Air	9.67	-	[34]
WR-03	220-325	3D printed (SLM)	No	Air	93.82	-	[34]
WR-03	220-325	Commercial	No	Air	84.09	-	[34]
WR-3.4	280	3D printed	No	Air	12	-	[29, 30]
WR-2.2	325-500	3D printed (Polyjet)	Yes	Air	440	-	This Work
WR-1.5	500-750	Bulk micromachined	Yes	Air	80	-	[19]

360° phase shifter with 13-dB insertion loss over the 240–310-GHz frequency range. These MMIC solutions inherently suffer from high insertion loss and limited power handling capability [50], which may be critical factors for some applications. Commercially available THz control components (e.g., from Flann microwave [51]) are generally limited to mechanically tunable machined MPRWGs. Examples include variable attenuations operating at up to 500 GHz, having 30 dB of dynamic range, and 360° phase shifters operating at up to 330 GHz [51]. A hybrid approach, which combines MEMS and machined MPRWG technologies, has demonstrated a high-performance 500–550-GHz reconfigurable phase shifter, having only 3 dB of insertion loss, while avoiding mechanical tuning [52].

With the advantages that 3-D printing has to offer, Imperial College London has been investigating two different proof-of-principle tunable front-end component technologies: under mechanical and optical control. With the former, the first fully 3-D-printed tunable variable phase shifter was demonstrated by Gillatt *et al.* [53]. With this X-band exemplar, an FDM-printed dielectric-flap MPRWG phase shifter measured 142° of relative phase shift at 10 GHz. With the latter, an MPRWG vector modulator will be reported here, for the first time, with its hybrid module design and preliminary experimental measured results presented in the next section.

IV. HYBRID 3-D-PRINTED THZ IQ VECTOR MODULATOR

Combining semiconductor devices with potentially low-cost, high-performance passive guided-wave structures, to create at-carrier frequency control components, may prove to be an ideal solution for implementing affordable transceivers in future ubiquitous THz applications. To this end, this section presents a hybrid 3-D-printed IQ vector modulator.

The generic block diagram for the proposed IQ vector modulator is shown in Fig. 8. A 3-dB power divider equally splits the input signal power into two channels. In each channel, there is an optically controlled variable attenuator, implemented with an implanted slab of HRS. The Q-channel has an HRS slab that is 80 μm longer than the one in the I-channel, to provide an additional 90° of electrical delay at the design frequency of 411 GHz (midband for WR-2.2). Both channels have independent optical control of the photo-generation of electron–hole pairs within their slab of HRS. The I and Q channel signals are then combined with an identical 3-dB power combiner. Providing independent control of the I and Q channels allows for the generation of potentially arbitrary IQ vectors within one quadrant. From this quadrant, selected vectors will provide the desired static constellation (e.g., for *M*-QAM signaling).

Fig. 9(a) shows the ANSYS high-frequency structure simulator (HFSS) electromagnetic model of the vector modulator design. The IQ vector modulator employs air-filled WR-2.2 MPRWGs, having an internal cross section of 560 μm × 280 μm. Fig. 9(b) illustrates the complete hybrid module assembly, showing the implanted HRS slab, integrated packaged laser diodes and heat sink.

It was found that the 3-dB power couplers can operate with an almost equal power split across the entire 325–500-GHz band. The I and Q channels are of equal physical length, having a spatial separation defined by the size of the laser diodes (which provide the optical control for the variable attenuators) housed in the upper split-block part.

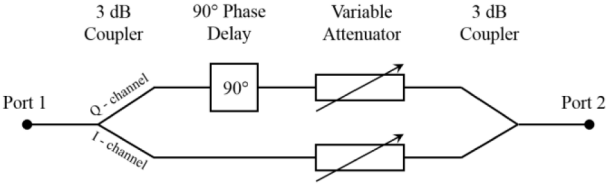

Fig. 8. *Generic IQ vector modulator block diagram.*

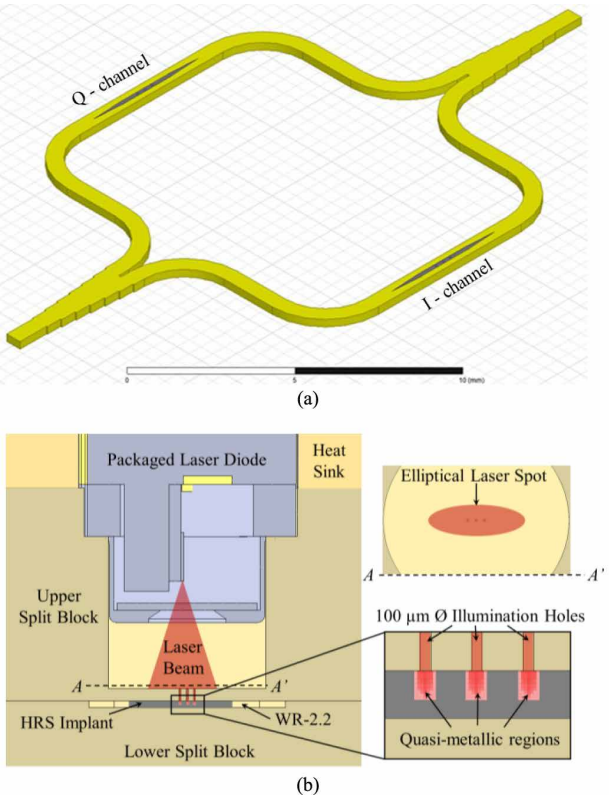

Fig. 9. ***Design of the THz vector modulator: (a) HFSS model showing the MPRWG structures (yellow) with HRS implants (gray); and (b) cross-sectional illustration of the complete hybrid module assembly.***

With implanted HRS slabs, simulations show that the loaded-MPRWG sections give an additional electrical delay of 0.89°/μm and 1.35°/μm at 325 and 500 GHz, respectively. When illuminated by the laser, the photo-generation of electron–hole pairs increases the conductivity of the exposed volume of HRS, thus, increasing the materials effective loss tangent, which in turn attenuates the THz electromagnetic wave as it propagates through this region. By controlling the level of constant current source supplying the laser [54], the level of incident power on the HRS can be varied, realizing an optically controlled variable attenuator.

For variable attenuation, the near-infrared (NIR) illumination source [laser diode or light-emitting diode (LED)] needs to have a free-space wavelength $\lambda < hc/E_g$, where h is Planck's constant, c is the speed of light in vacuum, and $E_g = 1.1$ eV is the bandgap energy of silicon; giving $\lambda = 1.1$ μm for HRS [51]. Therefore, a pair of Thorlabs LD830-ME2W, 830-nm 2-W lasers [54] were chosen to provide ample illumination for the IQ vector modulator. It has been shown by Zhou and Lucyszyn [55] that a longer wavelength moves the conductivity peek deeper within the HRS slab, requiring less laser power.

The results from full-wave electromagnetic simulations of all the waveguide components (using HFSS) were combined with idealized variable attenuation blocks (in AWR Microwave Office). This systems-level modeling was then used to predict the raw static constellation. The results at 420 GHz are shown in Fig. 10, with independently controlled attenuators swept between 0 and 20 dB.

The waveguide was realized as a split-block structure to allow easy insertion of the silicon slabs. The structure was 25 mm × 30 mm × 18.5 mm with integrated flanges and recesses to align the NIR laser diodes. It was found that the original SLA-printed parts suffered from shrinkage and bowing, leading to misalignments of the various features within both parts of the split block implementation. Huang *et al.* have shown that it is possible to compensate for shrinkage, but significant further work is required for these complex geometries [56]. For this reason, Polyjet printing was adopted (using our Stratasys Objet Connex 350 printer) having no observed shrinkage. To achieve the maximum spatial resolution, the two print heads were loaded with the same photopolymer, giving a quoted maximum resolution of 16 μm × 20 μm ×20 μm.

The Polyjet-printed parts are encased in a wax-like support material, which can be seen in Fig. 11(a). This is first mechanically removed, then cleaned in an ultrasonically agitated bath of isopropanol and finally polished with grade 3000 sandpaper. These cleaned parts were sputter coated with 500 nm of copper, which exceeds five skin depths at the lowest frequency of operation, minimizing conductor loss. A 30-nm-thick flash coating of gold was then sputtered on top to mitigate against copper oxidation. In order to avoid reaching the glass temperature of the polymer, multiple sputter coatings had to be undertaken, within short durations, and with time in-between for cooling. Sputtering was applied to both sides of the printed parts. The upper part, housing the

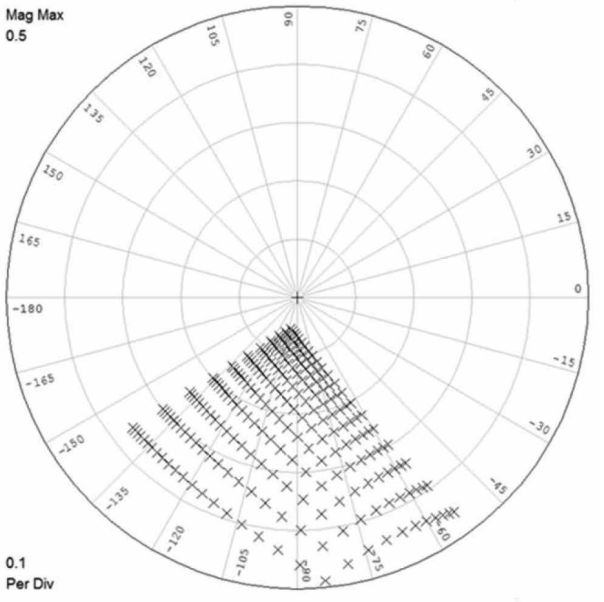

Fig. 10. ***Predicted IQ vector modulator raw static constellation at 420 GHz.***

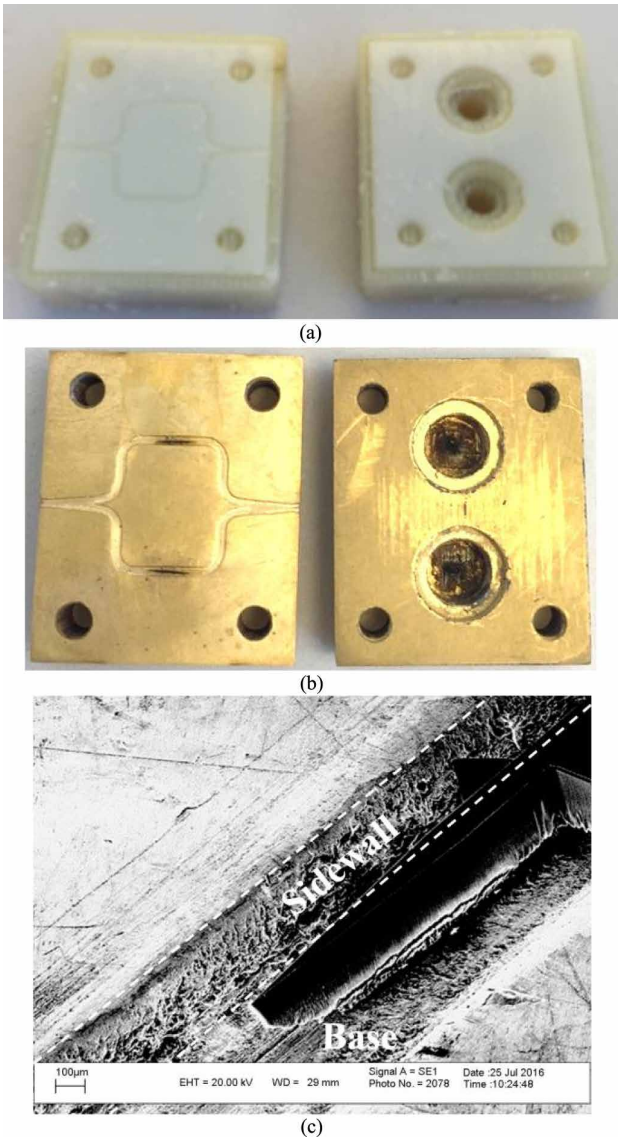

Fig. 11. ***Hybrid 3-D-printed THz IQ vector modulator module: (a) Polyjet-printed parts, encased in the wax-like support material; (b) after cleaning and plating; and (c) closeup view of the 100-μm-wide HRS slab, having a straight section of either 2.00 or 2.08 mm and 1.16-mm-long tapers at each end; each transverse fin is 20 μm wide and reaches out to 230 μm.***

packaged laser diodes, was then finished with laser machining of two sets of three 100-μm diameter holes, needed to illuminate the HRS slabs with the incident NIR beams but with minimal THz signal leakage. The final parts are shown in Fig. 11(b). Lips and alignment marks can be seen where the laser diodes sit within the upper part; this is to ensure that the elliptical beam of the laser is in the center of the recess and perfectly aligned above the implanted HRS slabs.

The silicon implants were manufactured from a 525-μm-thick, 100-mm diameter HRS wafer (having a resistivity >10 k/Ω.cm). First, the wafer is thinned to 270 μm, using an isotropic plasma etch. A backing wafer was temporarily applied to support the thinned wafer onto which a 10-μm-thick layer of AZ9269 photoresist was spun. The pattern of the slabs was transferred using standard photolithography [28]. The thinned wafer was then etched through completely and separated using acetone and Shipley Microposit remover 1165. The finished slabs were then secured within their respective MPRWG channel, as seen in Fig. 11(c).

S-parameter measurements were carried out using a Rohde and Schwarz ZVA vector network analyzer and a pair of Z-500 WR-2.2 downconverter test heads. Reference planes at the flanges were defined across the full waveguide band, by use of the recommended Thru, Offset short, Short and Match (TOSM) calibration algorithm. The fully assembled hybrid 3-D-printed THz IQ vector modulator was then clamped between the WR-2.2 measurement test heads, as shown in Fig. 12, using a pair (on each flange) of precision steel alignment pins (defined by the associated waveguide flange standard). Note that an additional copper heat sink is located at the top of the module to cool down the lasers.

The measured S-parameters of the IQ vector modulator, without and with (no optical illumination) the implanted HRS slabs, is shown in Fig. 13. With silicon implanted, there is a slight degradation in the input return loss, as one would expect. However, the insertion loss improved. This is because more of the energy is concentrated within the low loss silicon, away from the high surface resistance sidewalls. An operating frequency of 500 GHz was chosen. At this frequency, as seen in Fig. 13, the return loss and the insertion loss are both near their optimal values (around 20 dB).

From these measurements, the power of each laser was independently swept from the lasers turn-on current of 0.7–1.1 A, in course steps of 100 mA, resulting in a raw static constellation having only 25 vectors, shown in Fig. 14. From a raw static constellation, it is standard practice with nonideal IQ vector modulators to pick out the closest vectors to the symbol locations within the target constellation [44], minimizing the error vector magnitude (EVM); the associated set

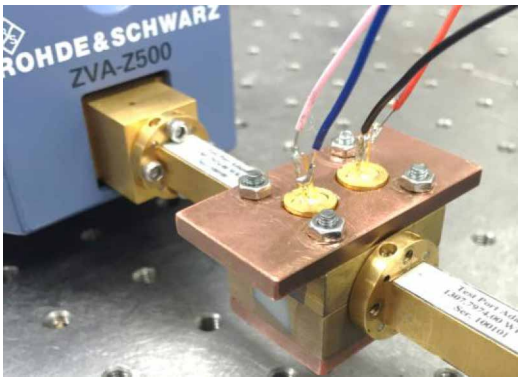

Fig. 12. ***Measurement setup for the fully assembled hybrid 3-D-printed THz IQ vector modulator module.***

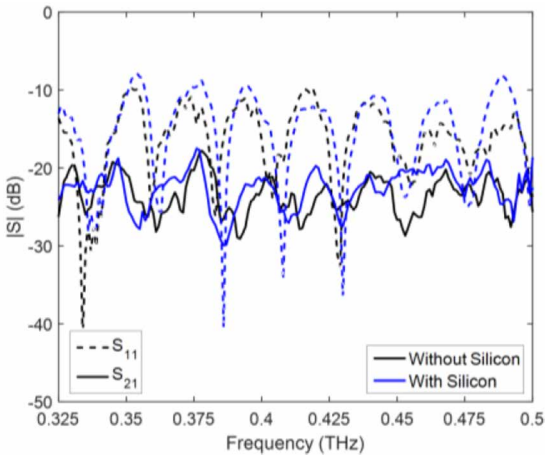

Fig. 13. *S-parameter measurements of the experimental proof-of-principle THz vector modulator, without and with (no optical illumination) the implanted HRS slabs.*

of unique bias points can then be stored in a lookup table, for retrieval during operation. In the same way, a 4-QAM constellation can be created, seen with the colored markers in Fig. 14. Obviously, smaller steps in the biasing of both lasers will result in many more vectors to choose from, leading to lower values of EVM and/or higher levels of *M*-QAM.

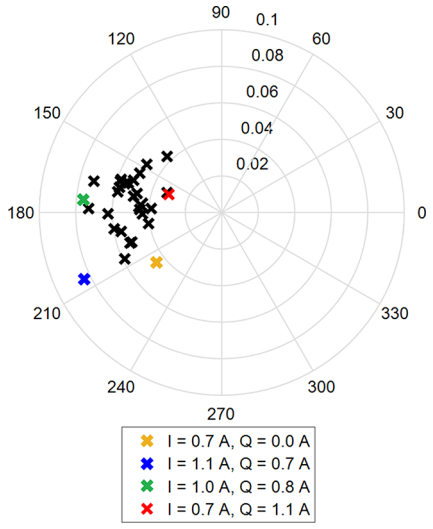

Fig. 14. *Preliminary S-parameter measurements of the experimental proof-of-principle THz vector modulator at 500 GHz. The raw static constellation has 25 unique vectors. A 4-QAM constellation is created by selecting the four vectors having colored markers (with associated laser bias currents given in the key).*

V. CONCLUSION

Three-dimensional printing for THz applications is still in its infancy. However, with the rapid pace of developments in all aspects of additive manufacturing technology (e.g., 3-D printing concepts, mechanical precision and material science), all indicators point to a positive spiral of advancement that will lead to ever-greater levels of performance and lower costs.

As a brief summary, for THz applications, it has been shown that: 1) FDM suffers from poor print resolution; 2) SLA has issues of shrinkage and bowing, which may be compensated for with full characterization from a stable process; 3) PolyJet currently provides the best solution; and 4) SLS/SLM has large surface roughness and requires costly post-processing.

Furthermore, a hybrid approach that combines semiconductor devices with 3-D-printed passive components represents a paradigm shift, which may prove to be an ideal solution for implementing affordable transceivers in future ubiquitous THz applications. With this in mind, the proof of principle for an experimental THz IQ vector modulator has been demonstrated and reported here for the first time. While only preliminary measurements have been given, it is clear that these measurements represent the current state of the art, in terms of both upper frequency limit (500 GHz) for 3-D-printed MPRWGs and functionality (optically tunable front-end control component), from which future implementations can be compared. Indeed, at the current rate of advancement in additive manufacturing, the authors predict that high-performance tunable front-end control components (and indeed other circuits, such as detector, mixers, amplifiers, oscillators, etc.) will be demonstrated above 1 THz within the next five years. ■

Acknowledgements

The authors would like to thank R. Siddle and Dr. M. Kovac for Polyjet printing of the WR-2.2 parts, within the Department of Aeronautical Engineering, Imperial College London; Prof. A. S. Holmes, J. Sun, Dr. G. Dou, and Dr. M. M. Ahmad for their assistance and guidance in manufacturing and measuring the WR-2.2 components, within the Department of Electrical and Electronic Engineering, Imperial College London; and Prof. N. Klein within the Centre for Terahertz Science and Engineering for access to THz metrology, within the Department of Materials, Imperial College London.

REFERENCES

[1] P. H. Siegel, "Terahertz technology," *IEEE Trans. Microw. Theory Techn.*, vol. 50, no. 3, pp. 910–928, Mar. 2002.

[2] T. G. Phillips and J. Keene, "Submillimeter astronomy," *Proc. IEEE*, vol. 80, no. 11, pp. 1662–1678, Nov. 1992.

[3] C. M. Armstrong, "The truth about terahertz," *IEEE Spectrum*, vol. 49, no. 9, pp. 36–41, Sep. 2012.

[4] M. Tonouchi, "Cutting-edge terahertz technology," *Nature Photon.*, vol. 1, no. 2, pp. 97–105, 2007.

[5] L. Li *et al.*, "Terahertz quantum cascade lasers with >1 W output powers," *Electron. Lett.*, vol. 50, no. 4, pp. 309–311, Feb. 2014.

[6] R. Han and E. Afshari, "A high-power broadband passive terahertz frequency doubler in CMOS," *IEEE Trans. Microw. Theory Techn.*, vol. 61, no. 3, pp. 1150–1160, Mar. 2013.

[7] K. Fukunaga, I. Hosako, Y. Ogawa, and S. Hayashi, "THz spectroscopy for art conservation science," in *Proc. 32nd Int. Conf. Infr. Millimeter Waves/15th Int. Conf. Terahertz Electon.*, Cardiff, U.K., Sep. 2007, pp. 678–679.

[8] M. Chakraborty *et al.*, "On the correlation of effective terahertz refractive index and average surface roughness of pharmaceutical tablets," *J. Infr., Millimeter, Terahertz Waves*, vol. 37, no. 8, pp. 776–785, Aug. 2016.

[9] K. Su, Y.-C. Shen, and J. A. Zeitler, "Terahertz sensor for non-contact thickness and quality measurement of automobile paints of varying complexity," *IEEE Trans. THz Sci. Technol.*, vol. 4, no. 4, pp. 432–439, Jul. 2014.

[10] R. Knipper *et al.*, "THz absorption in fabric and its impact on body scanning for security application," *IEEE Trans. THz Sci. Technol.*, vol. 5, no. 6, pp. 999–1004, Nov. 2015.

[11] A. D. V. Rheenen and M. W. Haakestad, "Robust identification of concealed dangerous substances by spectral correlation of terahertz transmission images," *IEEE Trans. THz Sci. Technol.*, vol. 5, no. 3, pp. 438–444, May 2015.

[12] I. F. Akyildiz, J. M. Jornet, and C. Han, "Terahertz band: Next frontier for wireless communications," *Phys. Commun.*, vol. 12, pp. 16–32, Sep. 2014.

[13] S. Lucyszyn, "The future of on-chip terahertz metal-pipe rectangular waveguides implemented using micromachining and multilayer technologies," in *IEE Colloq. Dig. Terahertz Technol. Appl.*, London, U.K., Apr. 1997, p. 10.

[14] S. Lucyszyn *et al.*, "Terahertz multi-chip module (T-MCM) technology for the 21st Century?," in *IEE Colloq. Dig. Multi-Chip Modules RFICs*, London, U.K., May 1998, pp. 6/16/8.

[15] G. Gallot, S. P. Jamison, R. W. McGowan, and D. Grischkowsky, "Terahertz waveguides," *J. Opt. Soc. Amer. B*, vol. 17, no. 5, pp. 851–863, May 2000.

[16] IEEE Standard for Rectangular Metallic Waveguides and Their Interfaces for Frequencies of 110 GHz and Above-Part 1: Frequency Bands and Waveguide Dimensions, IEEE Standard 1785.1-2012, 2012.

[17] IEEE Approved Draft Standard for Rectangular Metallic Waveguides and Their Interfaces for Frequencies of 110 GHz and Above-Part 2: Waveguide Interfaces, IEEE Standard 1785.2-2016, 2016.

[18] IEEE Approved Draft Recommended Practice for Rectangular Metallic Waveguides and Their Interfaces for Frequencies of 110 GHz and Above-Part 3: Recommendations for Performance and Uncertainty Specifications, IEEE Standard1785.3-2016, 2016.

[19] T. J. Reck, C. Jung-Kubiak, J. Gill, and G. "Chattopadhyay, Measurement of silicon micromachined waveguide components at 500–750 GHz," *IEEE Trans. THz Sci. Technol.*, vol. 4, no. 1, pp. 33–38, Jan. 2014.

[20] C. E. Collins *et al.*, "Micro-machined snap-together rectangular waveguide for terahertz circuits," in *Proc. IEEE 6th Int. Conf. Terahertz Electron.*, Sep. 1998, pp. 176–178.

[21] J. W. Digby *et al.*, "Fabrication and characterization of micromachined rectangular waveguide components for use at millimeter-wave and terahertz frequencies," *IEEE Trans. Microw. Theory Techn.*, vol. 48, no. 8, pp. 1293–1302, Aug. 2000.

[22] M. DAuria *et al.*, "3-D printed metal-pipe rectangular waveguides," *IEEE Trans. Compon. Packag. Manuf. Technol.*, vol. 5, no. 9, pp. 1339–1349, Sep. 2015.

[23] W. J. Otter and S. Lucyszyn, "3-D printing of microwave components for 21st century applications," in *Proc. IEEE MTT-S Int. Microw. Workshop Ser., Adv. Mater. Processes RF Terahertz Appl. (IMWS-AMP)*, Chengdu, China, Jul. 2016, pp. 1–3.

[24] R. Sorrentino and O. A. Peverini, "Additive manufacturing: A key enabling technology for next-generation microwave and millimeter-wave systems," *Proc. IEEE*, vol. 104, no. 7, pp. 1362–1366, Jul. 2016.

[25] S. F. Busch *et al.*, "Optical properties of 3D printable plastics in the THz regime and their application for 3D printed THz optics," *J. Infr., Millimeter, Terahertz Waves*, vol. 35, no. 12, pp. 993–997, Dec. 2014.

[26] J. Suszek *et al.*, "3-D-printed flat optics for THz linear scanners," *IEEE Trans. THz Sci. Technol.*, vol. 5, no. 2, pp. 314–316, Mar. 2015.

[27] X. S. Lu *et al.*, "Extrusion freeforming of millimeter wave electromagnetic bandgap (EBG) structures," *J. Rapid Prototyping*, vol. 15, no. 1, pp. 42–51, Jan. 2009.

[28] S. Lucyszyn, *Advanced RF MEMS*. Cambridge, U.K.: Cambridge Univ. Press, Aug. 2010.

[29] P. T. Timbie, J. Grade, D. van der Weide, B. Maffei, and G. Pisano, "Stereolithographed MM-wave corrugated horn antennas," in *Proc. 36th Int. Conf. Infr., Millimeter, Terahertz Waves*, Houston, TX, USA, Oct. 2011, pp. 1–3.

[30] A. Macor, E. de Rijk, S. Alberti, T. Goodman, and J.-P. Ansermet, "Note: Three-dimensional stereolithography for millimeter wave and terahertz applications," *Rev. Sci. Instrum.*, vol. 83, no. 4, Apr. 2012, Art. no. 046103.

[31] A. von Bieren, E. de Rijk, J.-P. Ansermet, and A. Macor, "Monolithic metal-coated plastic components for mm-wave applications," in *Proc. 39th Int. Conf. Infr., Millimeter, Terahertz Waves*, Tucson, AZ, USA, Sep. 2014, pp. 1–2.

[32] (Jul. 2016). [Online]. Available: http://www.swissto12.com/Products/Metal%20Coated%20Plastics/index.html

[33] Z. Wu, W. Ng, M. Gehm, and H. Xin, "Hollow-core electromagnetic band gap (EBG) waveguide fabricated by rapid prototyping for low-loss terahertz guiding," in *IEEE MTT-S Int. Microw. Symp. Dig.*, Anaheim, CA, USA, May 2010, pp. 644–647.

[34] Z. Wu, M. Liang, W.-R. Ng, M. Gehm, and H. Xin, "Terahertz horn antenna based on hollow-core electromagnetic crystal (EMXT) structure," *IEEE Trans. Antennas Propag.*, vol. 60, no. 12, pp. 5557–5563, Dec. 2012.

[35] P. Nayeri *et al.*, "3D printed dielectric reflectarrays: Low-cost high-gain antennas at sub-millimeter waves," *IEEE Trans. Antennas Propag.*, vol. 62, no. 4, pp. 2000–2008, Apr. 2014.

[36] S.-W. Qu, H. Yi, C. H. Chan, and K. B. Ng, "Low-cost discrete dielectric terahertz lens antenna using 3D printing," in *Proc. IEEE Conf. Antennas Meas. Appl.*, Antibes, France, Nov. 2014, pp. 1–3.

[37] K. Van Caekenberghe, P. Bleys, T. Craeghs, M. Pelk, and S. van Bael, "A W-band waveguide fabricated using selective laser melting," *Microw. Opt. Technol. Lett.*, vol. 54, no. 11, pp. 2572–2575, Nov. 2012.

[38] B. Zhang and H. Zirath, "Metallic 3-D printed rectangular waveguides for millimeter-wave applications," *IEEE Trans. Compon. Packag. Manuf. Technol.*, vol. 6, no. 5, pp. 796–804, May 2016.

[39] B. Zhang *et al.*, "Metallic 3-D printed antennas for millimeter-and submillimeter wave applications," *IEEE Trans. THz Sci. Technol.*, vol. 6, no. 4, pp. 592–600, Jul. 2016.

[40] F. J. Tischer, "Surface characteristics of metals and waveguide attenuation at millimeter-wave frequencies between 25 and 160 GHz," in *IEEE MTT-S Int. Microw. Symp. Dig.*, Jun. 1976, pp. 238–240.

[41] F. J. Tischer, "Experimental attenuation of rectangular waveguides at millimeter wavelengths," *IEEE Trans. Microw. Theory Techn.*, vol. 27, no. 1, pp. 31–37, Jan. 1979.

[42] B. Huang, J. Chen, and W. Jiang, "Effects of surface roughness on TE modes in rectangular waveguide," *J. Infr. Millimeter Terahertz Waves*, vol. 30, no. 7, pp. 717–726, Apr. 2009.

[43] W. R. McGrath, C. Walker, M. Yap, and Y.-C. Tai, "Silicon micromachined waveguides for millimeter-wave and submillimeter-wave frequencies," *IEEE Microw. Guided Wave Lett.*, vol. 3, no. 3, pp. 61–63, Mar. 1992.

[44] S. Lucyszyn, Q. H. Wang, and I. D. Robertson, "0.1 THz rectangular waveguide on GaAs semi-insulating substrate," *Electron. Lett.*, vol. 31, no. 9, pp. 721–722, Apr. 1995.

[45] S. Lucyszyn, D. Budimir, Q. H. Wang, and I. D. Robertson, "Design of compact monolithic dielectric-filled metal-pipe rectangular waveguides for millimetre-wave applications," *IEE Proc. Microw., Antennas Propag.*, vol. 143, no. 5, pp. 451–453, Oct. 1996.

[46] I. Stil *et al.*, "Loss of WR10 waveguide across 70116 GHz," in *Proc. 22nd Int. Symp. Space Terahertz Technol.*, Apr. 2012, pp. 1–3.

[47] W. J. Otter, S. M. Hanham, N. Klein, S. Lucyszyn, and A. S. Holmes, "W-band laser-controlled photonic crystal variable attenuator," in *Proc. IEEE MTT-S Int. Microw. Symp.*, Tampa, FL, USA, Jun. 2014. pp. 1–3.

[48] D. S. McPherson, H.-C. Seo, Y.-L. Jing, and S. Lucyszyn, "110 GHz vector modulator for adaptive software-controlled transmitters," *IEEE Microw. Wireless Compon. Lett.*, vol. 11, no. 1, pp. 16–18, Jan. 2001.

[49] C. Quan, S. Heo, M. Urteaga, and M. Kim, "A 275 GHz active vector-sum phase shifter," *IEEE Microw. Wireless Compon. Lett.*, vol. 25, no. 2, pp. 127–129, Feb. 2015.

[50] I. D. Robertson and S. Lucyszyn, Eds., *RFIC and MMIC Design and Technology*. London, U.K.: IEE Press, Nov. 2001.

[51] (Jul. 2016). [Online]. Available: http://www.flann.com/

[52] U. Shah *et al.*, "Submillimeter-wave 3.3-bit RF MEMS phase shifter integrated in micromachined waveguide," *IEEE Trans.*

THz Sci. Technol., vol. 6, no. 5, pp. 706–715, Sep. 2016.

[53] B. T. W. Gillatt, M. D'Auria, W. J. Otter, N. M. Ridler, and S. Lucyszyn, "3-D printed variable phase shifter," *IEEE Microw. Compon. Lett.*, vol. 26, no. 10, pp. 822–824, Oct. 2016.

[54] (Jul. 2016). [Online]. Available: https://www.thorlabs.de/thorproduct.cfm?partnumber=LD830-ME2W

[55] Y. Zhou and S. Lucyszyn, "Modelling of reconfigurable terahertz integrated architecture (RETINA) SIW structures," *Proc. PIERS*, vol. 105, pp. 7192, 2010.

[56] Q. Huang, J. Zhang, A. Sabbaghi, and T. Dasgupta, "Optimal offline compensation of shape shrinkage for three-dimensional printing processes," *IIE Trans.*, vol. 47, no. 5, pp. 431–441, 2015.

ABOUT THE AUTHORS

William J. Otter (Member, IEEE) received the M.Eng. degree in electrical and electronic engineering and the Ph.D. degree from Imperial College London, London, U.K., in 2010 and 2015, respectively.

During his M.Eng. degree he undertook industrial placements with BAE Systems, Advanced Technology Centre, Great Baddow, U.K., and held an IET FUSE scholarship. Throughout his Ph.D. he held the Val O'Donoghue Scholarship in the Department of Electrical and Electronic Engineering. He is currently a Postdoctoral Research Associate at Imperial College London, working in the area of millimeter-wave and THz biosensors. His current research interests include 3-D printing, photonic crystals, low-cost terahertz devices, electromagnetic modeling, optoelectronics, and electromagnetic sensors.

Stepan Lucyszyn (Fellow, IEEE) received the Ph.D. degree in electronic engineering from King's College London, University of London, London, U.K., in 1992 and the D.Sc. (higher doctorate) degree in millimeter-wave and terahertz electronics from Imperial College London, London, U.K., in 2010.

After working in industry as a satellite systems engineer for maritime and military communications, he went into academia. He is a Professor of Millimetre-Wave Systems and Director of the Centre for Terahertz Science and Engineering, Imperial College London. He has coauthored approximately 200 papers and 12 book chapters in applied physics and electronic engineering. He cofounded the Imperial College London spinoff company Drayson Wireless Ltd, *est.* Apr. 2014.

Prof. Lucyszyn was appointed an IEEE Distinguished Microwave Lecturer (DML) (2010–2012) and Emeritus DML (2013) in 2009. In 2011, he was the Chairman of the 41st European Microwave Conference, Manchester, U.K. He is currently a European Microwave Lecturer (EML) for the European Microwave Association.